

Extraction and analysis of structural features in cloud radar and lidar data using wavelet based methods

M. Quante¹, G. Teschke², M. Zhariy³, P. Maaß³, and K. Sassen⁴

¹GKSS Research Center, Institute for Coastal Research, Geesthacht, Germany

²Mathematics Department, Princeton University, Princeton, USA

³Zentrum für Technomathematik, University of Bremen, Bremen, Germany

⁴Geophysical Institute, University of Alaska, Fairbanks, USA

Abstract. Active remote sensing (i.e. the combination of cloud radar and lidar) is capable to capture the morphology of cloud fields as well as cloud internal structure. The GKSS 95 GHz cloud radar and the University of Utah high resolution lidar system have been used for studies on the internal structure and boundaries of altostratus clouds, cirrus, and frontal cloud systems. Some of the data were the basis for the development and tests of wavelet based methods for the detection of typical cloud features like complex boundaries, generating cells, fallstreaks, and dominant eddies. Many structural and dynamical signatures often remain undetected in larger data sets, since they live on scales which often are hidden in the quicklook type of inspection frequently applied. For dedicated studies these signatures need to be located and extracted. Wavelets can be useful for this task, i.e. one- and two-dimensional dyadic wavelet analysis is well suited for a fast multiscale analysis of the mostly non-periodic data. Fast analysis tools will become important when the amount of available data will increase as it is expected for the upcoming active remote sensing networks and planned spaceborne cloud radars. The overall goal therefore is to develop semi-automatic procedures to detect, locate and size characteristic cloud elements within large data sets. Illustrating first examples of our studies are presented here.

1 Introduction

Clouds strongly modify the radiation budget of the earth, i.e. the surface energy budget as well as the atmospheric heating and cooling profiles depend on the location and layer structure of clouds. One of the most striking features of clouds is their tremendous inhomogeneity on many scales. These scales are often coupled by dynamics and thermodynamics leading to a great deal of internal structure and to the, in general, inhomogeneous macrophysical appearance. Despite of this fact, in many models clouds are treated as plan parallel. Detailed information on the internal structure of cloud sheets

is of importance for the development of strategies and codes for more realistic computations of radiative transfer through inhomogeneous clouds. Information on predominant structures can also be very useful for the determination of underlying processes influencing the life cycle of clouds.

Cloud systems cover a large range of scales from kilometres down to the level of small droplets and crystals. Modern active remote sensing instruments are capable to obtain high resolution data from non-precipitating clouds. The analysis of this data is necessarily automated or examples are depicted on the basis of quick looks, which often are based on severely averaged data. During this process many interesting features in the structure of the signals remain undetected. There is a need to develop detection and analysis tools to make more use of the information contained in the high resolution data sets.

GKSS Research Center operates a 95 GHz (3.2 mm) cloud radar. The narrow beam width of the antenna, short pulse lengths, and the high pulse repetition frequency allow for high resolution profiling of stratiform clouds. The system has been used for studies on the internal structure and boundaries of stratus clouds, cirrus, and frontal cloud systems. The high resolution polarization diversity lidar of the University of Utah is also well suited to resolve small scales, i.e. in ice clouds. It has been used during several field campaigns to gather information among others on structural details of cirrus clouds and contrails.

The data sets are a profound basis for the development and test of wavelet based tools for the detection and sizing of typical cloud features. In general, the information in the signal is carried by irregular structures and transient phenomena, which are not easy to identify by standard methods. One- and two-dimensional continuous and dyadic wavelet analysis is well suited for a multiscale analysis of non-periodic data, where the dyadic multiscale analysis is computational more efficient. Fast analysis tools will become even more important, when the amount of available data will increase as it is expected when planned spaceborne cloud radars and lidars (Stephens et al., 2002; ESA, 2001) will go into orbit. Here we describe first steps which employ wavelet analysis

in order to locate and size characteristic clouds elements. The final goal of the study is to develop tools which allow for advanced data analysis and statistical treatment of information on cloud structure.

2 Wavelet analysis

The wavelet transform arose as an analysis tool capable of providing knowledge about a signal simultaneously in time/space and frequency/scale. The continuous wavelet transform was introduced in order to overcome the limited time-frequency localization properties of Fourier methods for non-stationary signals (Daubechies, 1992; Strang, 1993; Chui, 1997; Perrier et al., 1995; Vetterli and Kovacevic, 1995; Louis et al., 1998; Mallat, 1998). Wavelet analysis has been successfully used for many geophysical applications and in fluid dynamics, i.e. in the field of turbulence, (e.g. Abry 1997; Farge et al., 1996, 1999; Fofoula-Georgiou and Kumar, 1994; Gollmer et al., 1995; Kumar and Fofoula-Georgiou, 1997; Quante and Yamada, 1992; Torrence and Compo, 1998; Yamada and Ohkitani, 1991).

The 1-d. wavelet transform correlates the signal with a shifted and translated test function ψ , ($a, b \in \mathbb{R}, a \neq 0$):

$$W_{\psi}f(a, b) = |a|^{-1/2} \int_{\mathbb{R}} f(t)\psi\left(\frac{t-b}{a}\right)dt \quad (1)$$

The parameter a determines the scale (or size of details) which is examined. If the test function satisfies the admissibility condition

$$0 < c_{\psi} := 2\pi \int_{\mathbb{R}} \frac{|\hat{\psi}(\omega)|^2}{|\omega|} d\omega < \infty \quad (2)$$

it is called a wavelet and the transform (1) is invertible. Some standard examples for wavelets are the Haar wavelet (step function), the ‘‘Mexican hat’’ or Marr wavelet (second derivative of the Gaussian), the Morlet wavelet, or the Daubechies wavelets (see for example Daubechies, 1992; Chui, 1997). The choice of a suited wavelet is an important step at the beginning of the analysis. Our problem of evaluating radar measurements falls in the class of problems, for which the information searched for is contained in details/structures of yet unknown size and shape. The wavelet transform allows, due to its bandpass filtering property, to scan the signal on different frequency bands or detail scales simultaneously. In the case of radar measurements we suppose that the desired information (generation cells, fall streaks etc.) is contained on different scales. Further, we have to extend our setting to the continuous 2-d wavelet framework. The 2-d wavelet transform is defined by

$$W_{\psi}f(R, a, b) = |a|^{-1/2} \int_{\mathbb{R}^2} f(t)\psi\left(R\left(\frac{t-b}{a}\right)\right)dt, \quad (3)$$

where a is again a dilation parameter, $b \in \mathbb{R}^2$ and the rotation matrix $R \in SO(2)$. If the analyzing wavelet is rotation invariant then there is no chance to detect angular dependent information. The search for wavelets with optimal

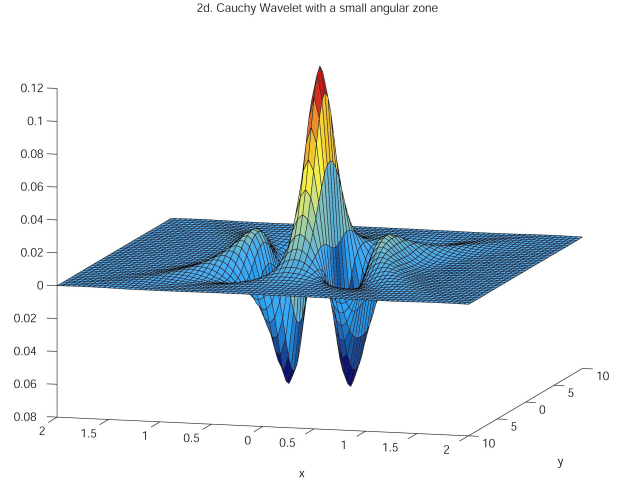


Fig. 1. Cauchy wavelet with a small angular zone for two dimensional analysis.

angular resolution is given by minimizing solutions of an angular uncertainty relation. One of these wavelets is the so-called Cauchy wavelet (Teschke, 1998) which is defined by its Fourier transform:

$$\hat{\psi}_{l,m}^{C,\eta}(\mathbf{k}) := \begin{cases} (\mathbf{k} \cdot \mathbf{e}_{\alpha})^m (\mathbf{k} \cdot \mathbf{e}_{\beta})^l e^{-\mathbf{k} \cdot \boldsymbol{\eta}} & \text{for } \mathbf{k} \in C(\alpha, \beta) \\ 0 & \text{otherwise} \end{cases} \quad (4)$$

with $\boldsymbol{\eta} \in C$ (angular resolution cone) and $l, m \in \mathbb{N}$. The time-domain representation of this wavelet used in our numerical test calculation is therefore given by:

$$\psi_{l,m}^{C,\eta}(\mathbf{x}) = (-1)^m \frac{(-i)^{l+m+2}}{2\pi} m l \sin^{l+m+1} \left(\frac{1}{(\beta - \alpha) [(\mathbf{x} + i\boldsymbol{\eta}) \cdot \mathbf{e}_{\alpha}]^{l+1} [(\mathbf{x} + i\boldsymbol{\eta}) \cdot \mathbf{e}_{\beta}]^{m+1}} \right) \quad (5)$$

This construction is based on minimizing an uncertainty relation, which measures the resolvable angular distance between different objects. The basic idea of constructing wavelets via uncertainty principle is the analogue of the famous Weyl-Heisenberg uncertainty relation, which may be interpreted as the uncertainty of localizing in time and phase simultaneously. The interpretation of the 1-d affine uncertainty is the localization in time and scale. For our purpose, the detection of anisotropic patterns in radar reflectivity and Doppler velocity measurements, the underlying principle was the 2-d time-angle uncertainty relation. Figure 1 shows as an example for an analysis function the 2-d Cauchy wavelet in physical space.

3 Measurements and data processing

3.1 Instruments

The data analysed for this study were taken by a groundbased millimeter wavelength cloud radar and a high resolution polarimetric lidar, which are briefly characterized below.

Cloud radar MIRACLE: The GKSS Research Center operates a transportable 95-GHz scanning cloud radar. The pulsed radar has a peak power of 1.7 kW, it is fully polarimetric and dopplerized. Pulse repetition frequency (up to 80 kHz), number and location of range gates, pulse width and pulse polarisation are selectable and allow for a range resolution between 7.5 m and 82.5 m up to a range of 15 km. The beamwidth of the centerfed Cassegrain antenna of 0.17° leads e.g. to a range cell diameter of 30 m at a distance of 10 km. The minimum sensitivity at an altitude of 1 km and 1 s integration time is about -40 dBZ. A more comprehensive description of the radar is given in Quante et al. (1998). The GKSS radar has been used for studies related to the structure and properties of layer clouds (e.g. Danne et al., 1999; Fujiyoshi et al., 1999; Quante et al., 2000). The measurements presented here were taken over Geesthacht, Germany, in an upward looking mode.

Polarization Diversity Lidar (PDL): The University of Utah at Salt Lake City operated a dual-wavelength scanning polarization diversity lidar (PDL). The PDL is a high-resolution device: it can record the four polarization channels (at the 0.532 and 1.064 m wavelengths) at a maximum resolution of 1.5 m and a PRF of 10 Hz (Sassen, 1994). The measurements used here were obtained during the SUCCESS field phase, which took place at the ARM Cloud and Radiation Testbed (CART) in Oklahoma, and were taken vertically pointing upward.

3.2 Wavelet computations

1-d continuous wavelet analysis

The one dimensional continuous wavelet transform (integral wavelet transform) can be used to analyze time/space series that contain nonstationary and non-periodic power contributions at many different scales. The term continuous refers also to the fact that the decomposition does not rely on an orthogonal basis. The scale resolution can be arbitrarily chosen. The transform provides only results for selected 1-d segments (along fixed range gates) of the underlying 2-d data sets. The implementation used for the present analysis follows that of Torrence and Compo (1998), the wavelet is convoluted in Fourier space with the data segment to be analyzed. Analysis functions used were the Marr wavelet and the complex Morlet wavelet. Results are presented in a so called scalogram, where the squared wavelet coefficients are plotted in a space/time-scale/period diagram. Their magnitude is colour coded.

2-d multiresolution analysis

The wavelet transform leads to the concept of multiresolution analysis (MRA) (Mallat, 1989), where images (or other signals) are decomposed into structures and then analysed at successive scales (or spatial-temporal resolutions). One approach consists of building a 2-d (x, y) multiresolution analysis simply by taking the direct (tensor) product of two

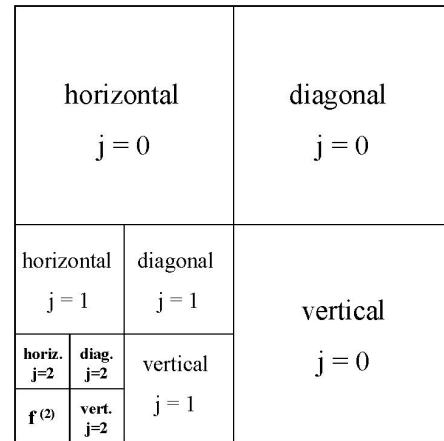


Fig. 2. Schematic representation of the visualisation of a hierarchical pyramid of a two dimensional wavelet transform based on multiresolution analysis (here a three scale analysis). The subplots show the wavelet components which emphasize, respectively, horizontal, diagonal, and vertical structures at scale j . The context image $f^{(j)}$ holds all scales larger than j .

such structures in 1-d, one for the x direction, one for the y direction. This 2-d analysis requires one scaling function but three wavelets for horizontal, diagonal, and vertical structures resulting from the scaling function and the basic wavelet in x and y directions. The actual computations are performed using a set of high and low pass filter coefficients which are applied to the data successively on each remaining scale in a discrete time/scale resolution (see, for example Mallat, 1989; Starck et al., 1998 for details). As basic wavelets the Haar and Daubechies-4 (Daubechies, 1992) – both orthogonal- and a biorthogonal spline wavelet (Chui, 1997) have been used for the decomposition. The B-spline wavelet has the advantage of being symmetric and has a better space-scale localisation compared to the Daubechies-4 wavelet. In most cases 5 iterations have been performed to decompose the 2-d data sets. Cyclic boundary conditions have been used, dedicated boundary wavelets (Chui, 1997) have not yet been implemented. The results are visualised in a hierarchical pyramid introduced in Fig. 2.

2-d continuous angular dependent analysis

For the angle resolving scale analysis non-symmetric 2-d wavelets with a small angular zone are employed. These wavelets were rotated at each position and moved through the data successively at each selected scale. The discrete angle resolution was pre-set. In most cases 10 different angels have been used uniformly distributed between 0 and 2π in a mathematically positive sense, with 0 pointing along the positive x axis. The angular sensitivity cone of the Cauchy wavelet ranged between $-\pi/18$ and $+\pi/18$. The multi-parameter results (scale, position and direction) can be presented in different ways. In Fig. 12 some of the ways are illustrated, they are explained in the figure caption.

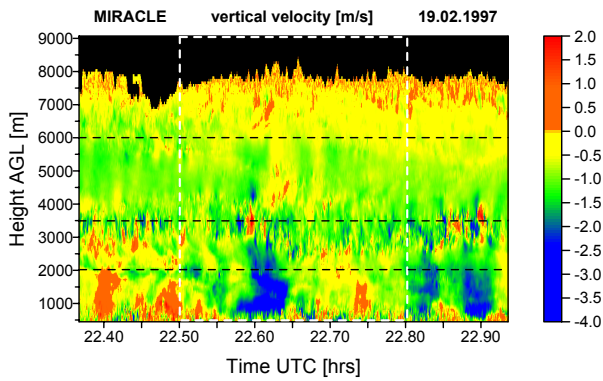


Fig. 3. Height time cross-section of the Doppler velocity measured by the GKSS cloud radar for a segment of a deep frontal cloud system passing Geesthacht on 19 February 1997. Negative velocities indicate downward motion.

4 Results

Three example cases have been selected in order to illustrate the type of results that can be expected from the localized space-scale analysis. In all three cases dynamically active regions are the phenomena looked for as they are of interest for cloud dynamical studies concerned with the development and life cycle of stratiform cloud layers. In all three cases the features have been detected more or less by chance, they were hidden in a pile of data collected during different measurement campaigns.

4.1 Strong dynamical coupling of two layers in a deep frontal system

Figure 3 shows a height-time section of the Doppler velocity observed during the passage of a frontal system over Geesthacht, Northern Germany, in the evening of 19 February 1997. This plot, representing about 38 minutes, shows the cloud conditions just after the passage of a warm front. The warm sector was very narrow, and the associated cold front passed the radar site about two hours later. Although the deep cloud system was very compact, some tops reached the 10 km level. Precipitation was not reaching the ground during the displayed time period, whereas the cold front later on lead to rain and snow as well as to strong and gusty winds. In most parts of the cloud there was slight downward motion, but numerous convective and turbulent active regions can be seen on small scales around 3 to 4 km altitude and, on even smaller scales, in the boundary layer below 1 km.

In the time interval discussed here, the deep convective situation broke up into a 4.5 km thick altostratus and a dense line of intense convective cloud cells below, whose tops were just touching the upper layers base. The interaction between the two cloud layers was very intense manifesting itself in an interlacing pattern of up and down drafts on a relatively small scale. The Doppler velocities ranged between -3 and $+2$ ms^{-1} . Note that the radar Doppler measurements gathered in an upward looking mode contain contributions from terminal

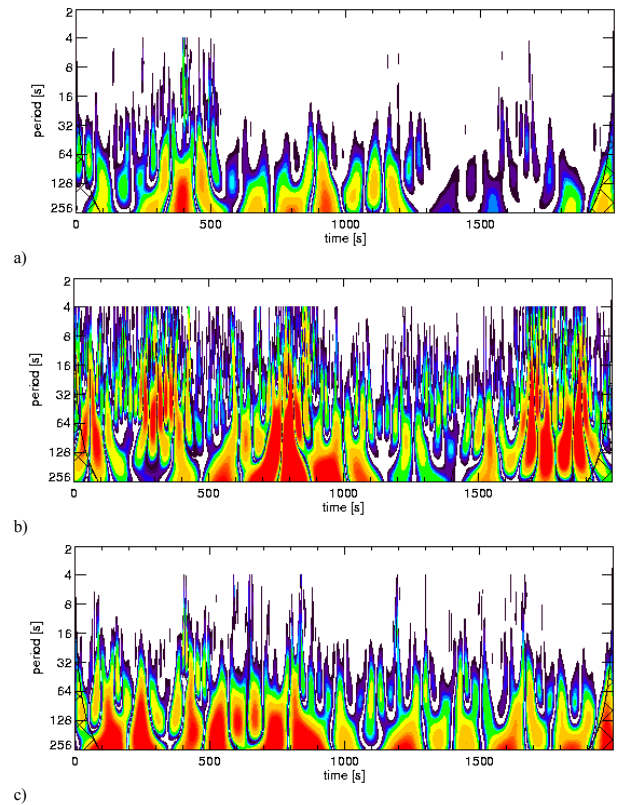


Fig. 4. Scalograms (time/period) of the squared wavelet coefficients (Marr wavelet) for the Doppler velocity signals along the horizontal dashed lines in Figure 3: (a) at 6 km (upper cloud layer), (b) at 3.5 km (coupling region), and (c) at 2 km altitude. The wavelet variance is colour coded increasing from blue to red with a lower threshold of $0.05 \text{ m}^2 \text{ s}^{-2}$ and an upper bound of $20 \text{ m}^2 \text{ s}^{-2}$.

velocities of the particles as well as from the vertical air velocity. The two distinct cloud layers were actually strongly coupled in such a way that led to enhanced particle growth due to transport of ice crystals into the lower liquid layers. Wavelet scalograms for three Doppler velocity series from range gates at 2 km, 3.5 km, and 6 km altitude, as indicated by the dashed horizontal lines in Fig. 3, are shown in Fig. 4a–c. The selected heights are located in the lower level precipitation cells, the coupling region, and just below a shear layer in a relatively calm part at cloud top. The analysing function adopted for the continuous analysis presented in the figure was a Marr wavelet. The same analysis using a Morlet wavelet led to a slightly different localisation of the events. Since during the measurements the cloud was traveling over the radar and might have undergone some changes during that time, the “position” parameter in the plot is given in units of time. Nevertheless, the mean horizontal distance covered by the data segment can be estimated to be around 28 km based on the horizontal wind at 4 km. The scale parameter is accordingly given as a period. Again, the period can be roughly translated to a length scale using the horizontal wind at the appropriate height level (10 , 12 , 18 ms^{-1} , respec-

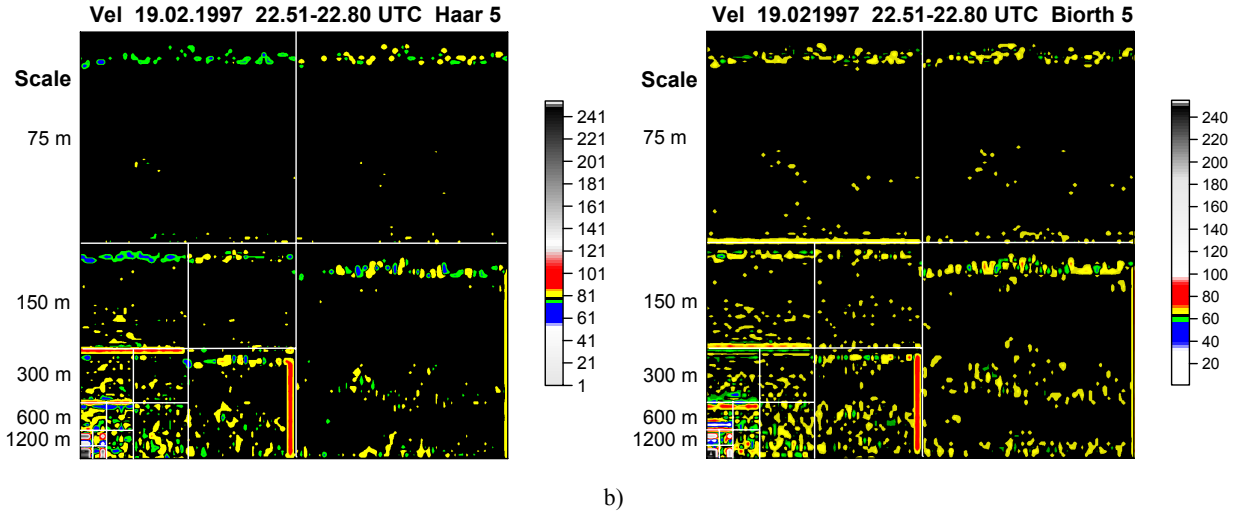


Fig. 5. Wavelet decomposition of the Doppler velocity measurements highlighted by the white frame in Fig. 3 into 5 multiresolution layers using (a) the Haar wavelet and (b) a biorthogonal spline wavelet. The results are scaled linearly into the range between 0 and 255, the magnitude of the MRA decomposition coefficients is colour coded so as to emphasize the details. The vertical scales are given on the left hand side, the horizontal scales match the vertical ones closely.

tively). In Fig. 4 the squared amplitude of the wavelet coefficients, representing the velocity variance, is colour coded increasing from blue to red with a lower threshold of $0.05 \text{ m}^2 \text{ s}^{-2}$ and an upper bound of $20 \text{ m}^2 \text{ s}^{-2}$. It can be seen that the variance distribution over the scales is strongly changing from level to level. While the upper cloud top region, as expected, is quite smooth, with some structures at larger scales ($> 1 \text{ km}$) in the first half of the series, the activity in the coupling region at most positions is distributed over all resolved scales from about 50 m to 3 km. Here an obvious band of mid size features centred around a scale of about 400 m (32 s period) marks the chain of up- and down drafts at this level. In the lower cloud layer most of the isolated structures size between 600 m and 1.2 km, again they are more intense in the first half of the record. Figure 5a and b present the wavelet decomposition of the Doppler velocity measurements highlighted by the white frame in Fig. 3 into 5 multiresolution layers using the Haar wavelet and a biorthogonal B-spline wavelet. Results obtained using the Daubechies-4 wavelet are not shown, they are qualitatively close to the ones with the B-spline wavelet, which has a slightly better location behaviour. The decomposition clearly detects the small scale events in the active regions of the cloud, namely at cloud top where generating cells are present, in the coupling region around 3.5 km, and in the boundary layer below 1.5 km. The small scale features are more pronounced in the vertical sub-plots (see Fig. 2 for sub-plot definitions). The comparison of Figs. 5a and b reveals a pronounced difference due to the wavelet used. Obviously, the Haar wavelet is more sensitive to edges and sharp gradients, this can be especially seen in the horizontal sub-plots, where at small scales the cloud boundary is generating the signal.

The wavelet coefficients from the continuous analysis have

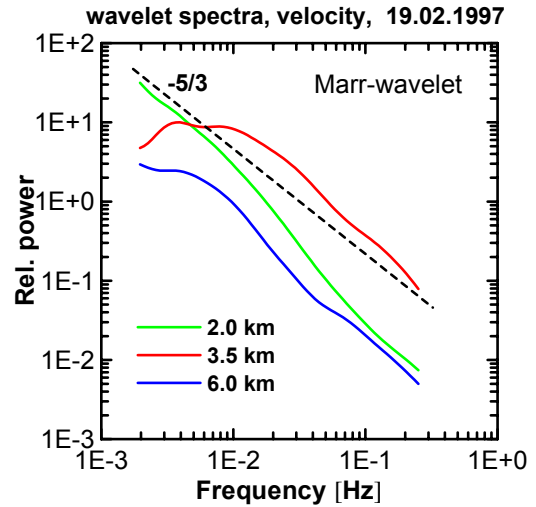


Fig. 6. Global wavelet spectra for Doppler velocities along the horizontal dashed lines in Fig. 3 calculated using the Marr wavelet. A $-5/3$ line is shown for orientation.

been used to calculate global power spectra for each selected height level, they are compared in Fig. 6. The resulting spectra show remarkably different power levels and roll-off behaviour, the one for the coupling layer has the highest power and rolls off with a slope close to $-5/3$ indicating the existence of a developed turbulence cascade. The spectrum for 2 km shows a pronounced scale break in the middle of the resolved frequency range. This is due to an uneven distribution of the dominant power along the height band as visible in Figs. 4 and 5. Without the information of the position resolving wavelet decomposition this type of global spectra

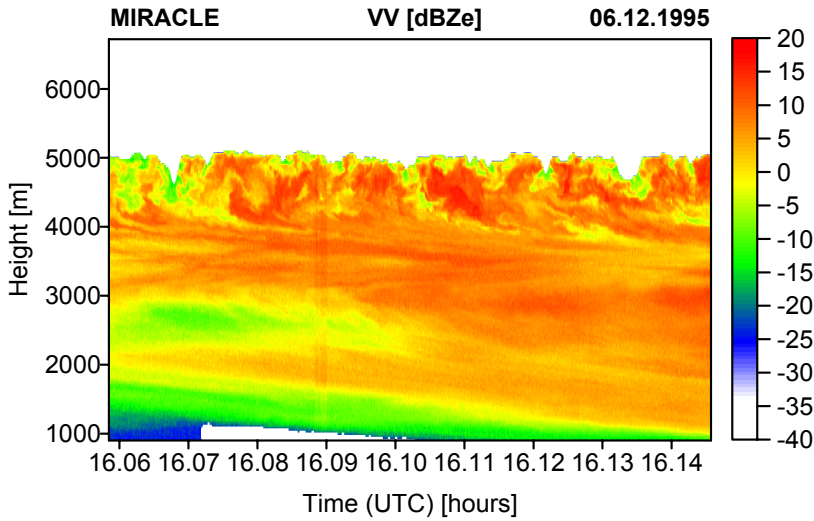


Fig. 7. Height time cross-section of the equivalent reflectivity factor measured by the GKSS cloud radar for a segment of a deep ice cloud layer passing Geesthacht, Germany, on 6 December 1995.

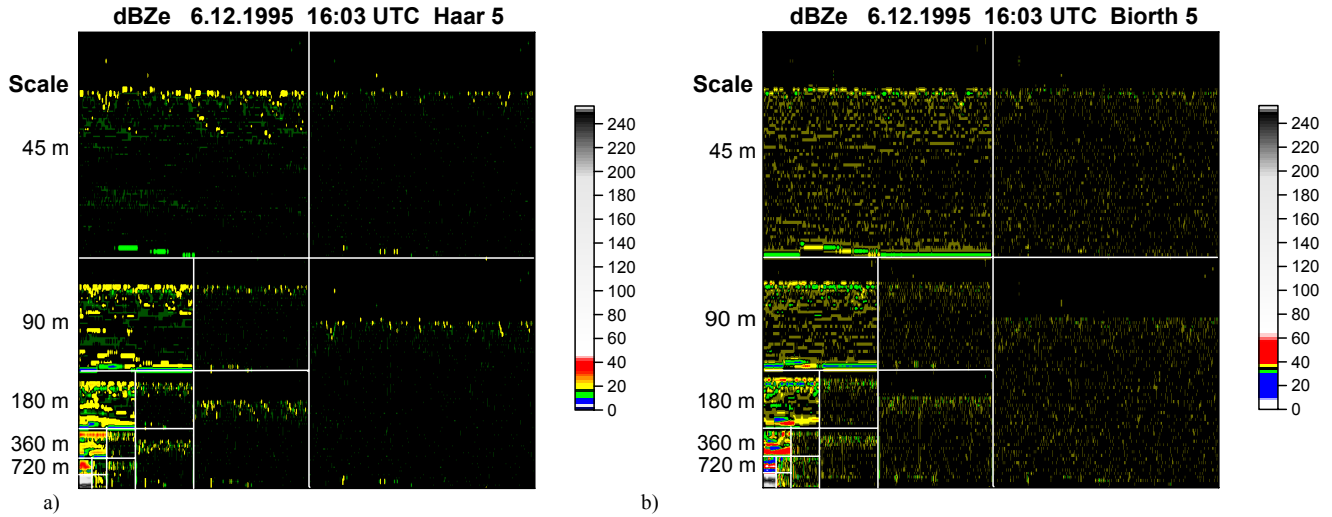


Fig. 8. As Fig. 5 but for the reflectivity data shown in Fig. 7.

(losing local information) could lead to false interpretations.

While the 1-d transform allows the sizing and positioning for selected heights, the 2-d transform provides additionally to sizing and positioning the main direction of the dominant events in the 2-d data plane. Small scale activity is confined to only a few areas in the cloud system, namely in the cloud top layer, the coupling region and the precipitation generation region, where the activities in the latter two areas more obvious in the vertical subplots.

4.2 Structure and dynamics of a deep stratiform ice cloud – generating cells

The capability of the radar to resolve meso- and microscale internal structures within stratiform clouds is highly illustrated by a cloud event observed on 6 December 1995, over Geesthacht. This deep, but non-precipitating cloud system covering large areas of Northern Germany occurred during

a high-pressure situation within a moderate easterly flow. Figure 7 shows the height-time cross section of the equivalent radar reflectivity (co-polarized signal, vv) for a time period of about 5 minutes. The vertical and temporal resolution were 30 meters and 0.2 seconds, respectively. The reflectivity pattern looks stratiform below 4 km, whereas significant structures on several scales together with fall streaks (marking the strong wind shear at that level) and an inhomogeneous cloud top can be seen further above. This pattern marks an unstable layer with convective activity and enhanced turbulence intensity, between 4.5 and 5 km. This unstable layer could indeed be identified in several radiosonde ascents over Northern Germany, indicating that there is a well defined link between these small-scale cloud features and the corresponding atmospheric conditions on much larger scales. Downward intrusion of dry air deep into the cloud is obvious and supported by the analysis of

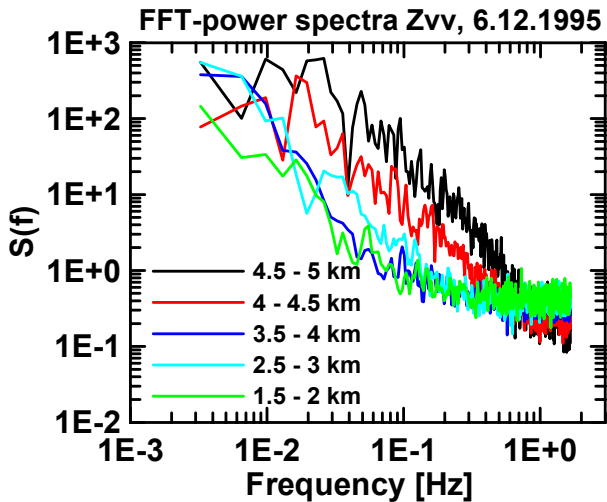


Fig. 9. Height band averaged FFT power spectra for the reflectivity data shown in Fig. 7.

Doppler data (not shown here). The whole life cycle of this cloud is dominated by the activities at cloud top. More aspects of this case study are discussed in detail by Fujiyoshi et al. (1999).

The 2-d multiresolution analysis, displayed in Fig. 8, of the reflectivities shown in Fig. 7 leads to the conclusion that beside some activity at cloud top most of the events contribute to the coefficients representing mainly horizontal signatures. The Haar analysis highlights the edges of fallstreaks on scales between the 45 m and 90 m, these can not adequately be seen in the B-spline decomposition. The latter in stead provides a good indication of the generating cells at cloud top existing on scales between 180 m and 360 m. Since the cells are uniformly distributed along the top, as supported by the wavelet results, conventional spectral analysis can also be used to characterize their sizes.

Figure 9 shows power spectra (each represents a mean over 16 single FFT-spectra for consecutive range gates) of reflectivity time series for selected height bands for the convective and the different stratiform regions in the cloud. Above 0.5 Hz (about the radar range cell resolution) the spectral amplitudes are highest in the convective region. Also clear evidence for a $-5/3$ power law is found for higher frequencies, indicating that the turbulence cascade causes the observed reflectivity distribution. The analysis of respective Doppler velocity spectra (not plotted here) supports this conclusion. The spectra for the upper two defined layers reveal a scale break between 0.04 and 0.05 Hz leading to the assumption that the turbulence is strongly connected to the generating cells in the cloud top region. The upper bound of the turbulence cascade is therefore given by the cell size which is less than about 400 m (using radiosonde winds for the time-space conversion) in accordance with results of the MRA presented above.

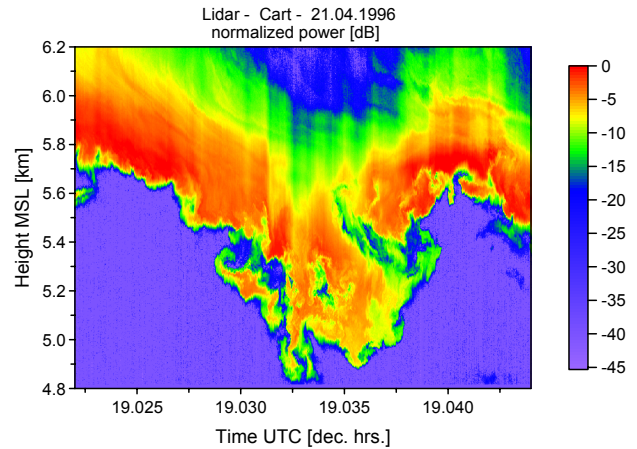


Fig. 10. A high resolution (1.5 m by 0.1 s) polarization diversity lidar display of a vigorous cirrus spissatus mammatta detected on 21 April 1996 from DOE CART site near Lamont, Oklahoma. The normalized power is given in dB.

4.3 Active cloud base of a multi-layer cirrus field

Figure 10 is a high resolution (1.5 m \times 0.1 s) PDL return power display of a particularly intense mammata protruding from the base of a dense cirrus fibratus cloud. This interesting plot represents a cross-section of a mammata that apparently passed directly above the lidar. It produced such strong optical attenuation that the lidar penetration depth was momentarily restricted to about 0.5 km in the 4.0 km deep spissatus layer. Attenuation led to the vertically oriented stripes in some parts of the upper cloud region. Note the depiction of various scales of turbulent eddies during their downward penetration into dry sub-cloud air. The measurements were made on 21 April 1996, during the SUCCESS field campaign in Oklahoma. The cloud segment shown was a part of the lowest base of a multi-layered cirrus system which occurred between about 5 km and 11.5 km.

Several such events appeared during the passage of the cloud field. The dynamical and thermodynamical conditions retrieved from a local radiosounding (Purcell, Oklahoma) lead to low Richardson numbers in the base region of 0.15 to 0.3 enabling self containing convection and maintaining turbulence. Possible reasons for the initial instabilities could be ice crystal sedimentation from higher layers or secondary generating cells driven by strong evaporation. Horizontal winds rose from 25 ms^{-1} to 30 ms^{-1} in the displayed height range of Fig. 10. The 2-d multiresolution analysis for the lidar backscatter data of this case is presented in Fig. 11 in the same way as for the two cases introduced above. It is very obvious that for both wavelets the smallest scales are sensitive to noise features outside the cloud boundaries (according to Fig. 10), these features start vanishing at larger scales. The Haar wavelet marks well the cloud edges at the 25 m scale. The pattern of cloud free air and cloud elements led to a complex cloud boundary which is well captured by the Haar wavelet, being most sensitive to sharp gradients. At

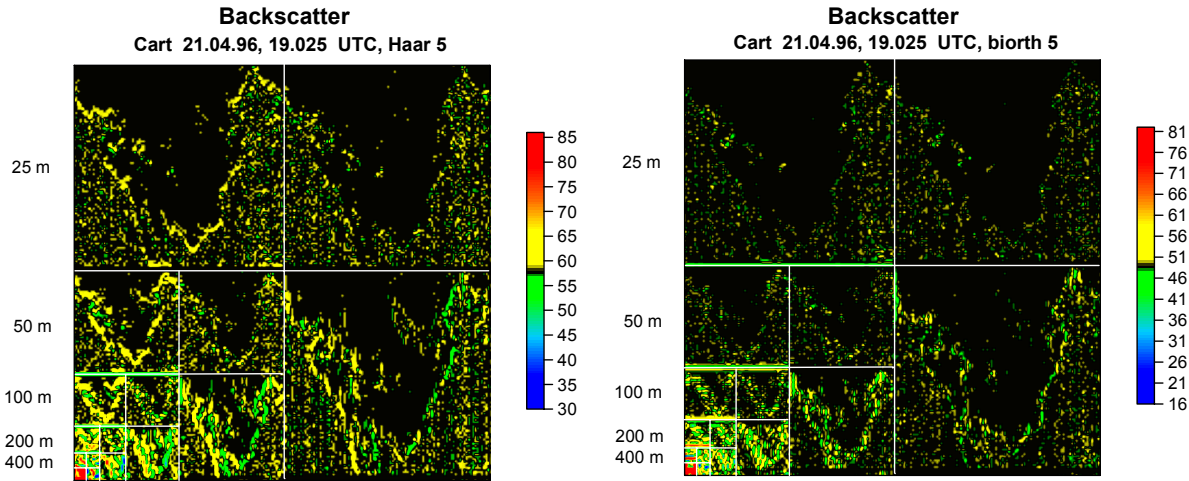


Fig. 11. As Fig. 5 but for the lidar data shown in Fig. 10.

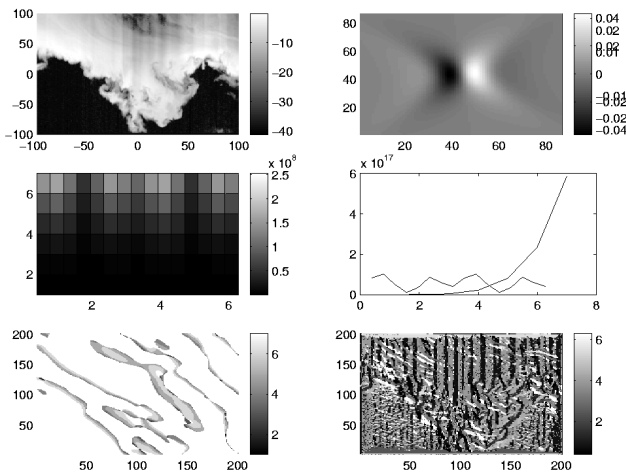


Fig. 12. Results of a continuous wavelet transform using a rotating analysis function for the lidar data shown in Fig. 10. (a) original data, (b), analysing wavelet: here affine 2-d Weyl-Heisenberg wavelet, (c) scale-angle indicator; left axis: scale 1 to 7, lower axis: angle 0 to 2π . Colours denote scale of dominating direction, (d) averaged information shown in (c) for the scale – lower curve – and for the angle – upper, exponential like curve –, (e) average over scales: display of direction dominating scales in space co-ordinates (f) dominating direction in space co-ordinates for a fixed fine scale.

smaller scales the B-spline wavelet is more sensitive to vertically oriented features in accordance with localized downward penetration into the subcloud air. At larger scales (> 100 m) this wavelet starts depicting the eddy like structures as the are visible in Fig. 10. This example underlines the importance of the right choice of the analysing wavelet, which needs to be carefully selected according to the expected results. In some cases the simultaneous use of different types of wavelets seems to be appropriate.

In extension to the MRA, for this example continuous 2-d transforms have been calculated using angular dependent

wavelets. A typical result using an affine Weyl-Heisenberg wavelet is shown in Fig. 12. The displayed subplots are explained in the figure caption. In Fig. 13 results applying an angular sensitive Cauchy wavelet to the data are provided, here only the dominating directions are plotted in a space co-ordinate system for two fixed fine scales. It is obvious that the directional information differs strongly between the scales. The vertical stripes (caused by attenuation, as explained above) are of course well detected. As cloud features diagonal fall streaks are visible with slightly varying directions as they move downward into a shear layer (some of them are not easy to spot in the original data). The eddies around the cloud edges are best captured on the smaller scale. The angular dependent analysis contains much information on the underlying dynamics, this calls for a more rigorous evaluation.

5 Conclusion

Many of cloud structural and dynamical features contained in remote sensing measurements, like those presented in this study, often remain undetected, because of the usual averaging procedures necessary for quick look type of data inspections. An advanced analysis tool should be capable to extract predefined features from the archived data sets. First tests using wavelet methods for the analysis of cloud radar and lidar data have been presented. One- and two-dimensional continuous and discrete wavelet analysis has been explored with the aim to detect, localise, and size typical structural features, which often are related to cloud dynamical processes.

Wavelets have shown to be useful for identifying active cloud regions like generating cells, eddies, and fall streaks. The examples examined underline the importance of the right choice of the analysing wavelet. It needs to be carefully selected according to the expected or searched for structures. In some cases the concurrent use of different types of wavelets seems to be appropriate (e.g. on different scales different

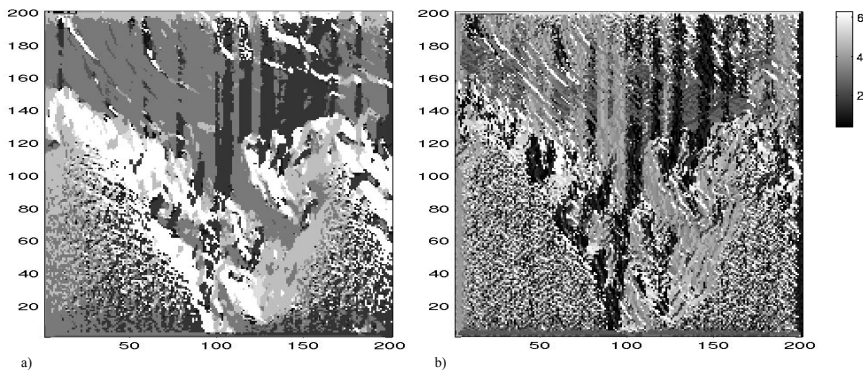


Fig. 13. Dominating directions in space co-ordinates (as in Fig. 12f) for two fixed fine scales using a 2-d Cauchy wavelet with small angular zone; (a) scale: 0.1 and (b) scale: 0.4.

analysis functions might be used). The discrete multiresolution analysis, although not resolving continuously all possible scales, has the advantage of being computationally very efficient.

Wavelet based algorithms seem to be suited for at least some of the tasks in connection with a more sophisticated data treatment. The scale-decomposition is only a first necessary step. Secondary scale dependent analysis procedures which evaluate the wavelet coefficient matrices still have to be developed and tested in order to reliably analyse high resolution radar and lidar data in a quasi-automated manner.

Acknowledgement. MQ thanks Olaf Danne for his help during the radar measurements and data processing and Prof. Michio Yamada, University of Tokyo, for inspiring initial discussions on wavelet analysis. KS acknowledges the help of Zhieng Wang of the University of Utah, Salt Lake City, in lidar data processing. We would also like to thank C. Torrence and G.P. Compo, ASP NCAR, for providing their 1-d wavelet code.

References

- Abry, P., 1997: *Ondelettes et turbulence*. Diderot, Paris, 292 pp.
- Chui, C.K., 1997: *Wavelets: A mathematical tool for signal analysis*. SIAM, Philadelphia, 210pp.
- Danne, O., M. Quante, D. Milferstädt, H. Lemke, and E. Raschke, 1999: Relationships between Doppler spectral moments within large-scale cirro- and altostratus cloud fields observed by a ground-based 95 GHz cloud radar. *J. Appl. Meteor.*, 38, 175-189.
- Daubechies, I., 1992: *Ten Lectures on wavelets*. SIAM CBMS 61, Philadelphia, PA, 357pp.
- ESA (European Space Agency), 2001: *The Five Candidate Earth Explorer Missions - EarthCare - Earth Clouds, Aerosols and Radiation Explorer*. ESA SP-1257(1), ESTEC, Noordwijk, The Netherlands, 130pp.
- Farge, M., N. Kevlahan, V. Perrier, and E. Goiraud, 1996: *Wavelets and turbulence*. *Proceedings of the IEEE*, 84, 639-669.
- Farge, M., N.K.-R. Kevlahan, V. Perrier and K. Schneider, 1999: *Turbulence analysis, modelling and computing using wavelets*. In Van den Berg, J.C., (ed.), 1999: *Wavelets in physics*. Cambridge University Press, Cambridge, 117-200.
- Foufoula-Georgiou, E., and P. Kumar, (eds.), 1994: *Wavelets in Geophysics*. Academic Press, San Diego, 373pp.
- Fujiyoshi Y, Quante M, Danne O, and Raschke E, 1999: *Properties of Deep Stratiform Ice Cloud Revealed by 95 GHz Cloud Radar - A Case Study*. *Contr. Atmos. Phys.*, 72, 113-125.
- Gollmer, S.M., Harshvardhan, R.F. Cahalen, and J.B. Snider, 1995: *Windowed and wavelet analysis of marine stratocumulus cloud inhomogeneity*. *J. Atmos. Sci.*, 52, 3013-3030.
- Kumar, P., and E. Foufoula-Georgiou, 1997: *Wavelet analysis for geophysical applications*. *Rev. of Geophys.*, 35, 385-412.
- Louis, A.K., P. Maaß, and A. Rieder, 1998: *Wavelets*. Teubner, Stuttgart, 330pp.
- Mallat, S., 1989: *A theory for multiresolution signal decomposition: the wavelet representation*. *IEEE Trans. Patt. Recog.*, and *Mach. Intell.*, 11, 674-693.
- Mallat, S., 1998: *A wavelet tour of signal processing*. Academic Press, San Diego, 577 pp.
- Perrier, V., T. Philipovitch, and C. Basdevant, 1995: *Wavelet spectra compared to Fourier spectra*. *J. Math. Phys.*, 36, 1506-1519.
- Quante, M., and M. Yamada, 1992: *Wavelet analysis of turbulence in cirrus clouds*. In B. Guillemet (ed.) *Fifth ICE/EUCREX Workshop*, Clermont-Ferrand, France, 47-57.
- Quante, M., Danne, O., Lemke, H., Milferstädt, D., and Raschke, E., *The GKSS 95-GHz cloud radar: system description and potential contributions in support of the Earth Radiation Mission*. ESA/ESTEC Report EWP-1968, 75-80, 1998.
- Quante, M., H. Lemke, H. Flentje, P. Francis, and J. Pelon, 2000: *Boundaries and internal structure of mixed phase clouds as deduced from ground-based 95-GHz radar and airborne lidar measurements*. *Phys. Chem. Earth*, 25, 889-895.
- Sassen, K., 1994: *Advances in polarization diversity lidar for cloud remote sensing*. *Proc. IEEE*, 82, 1907-1914.
- Starck, J.-L., F. Murtagh, and A. Bijaoui, 1998: *Image processing and data analysis: the multiscale approach*. Cambridge University Press, 287pp.
- Stephens, G. L., and co-authors, 2002: *The CloudSat mission and the EOS constellation: A new dimension of space-based observations of clouds and precipitation*. Submitted to *Bull. Amer. Meteorol. Soc.*
- Strang, G., 1993: *Wavelet transforms versus Fourier transforms*. *Bull. Amer. Math. Soc.*, 28, 288-305.
- Teschke, G., 1998: *Komplexwertige Wavelets und Phaseninformation, Anwendungen in der Signalanalyse*, diploma thesis, Potsdam.
- Torrence, C., and G.P. Compo, 1998: *A practical guide to wavelet analysis*. *Bull. Amer. Meteor. Soc.*, 79, 61-78.
- Vetterli, M., and J. Kovacevic, 1995: *Wavelets and subband coding*. Prentice Hall, New Jersey, 488pp.
- Yamada, M., and K. Ohkitani, 1991: *Orthonormal wavelet analysis of turbulence*. *Fluid Dyn. Res.*, 8, 101-115.